

QPOML: A Machine Learning Approach to Detect and Characterize Quasi-Periodic Oscillations in X-ray Binaries

Thaddaeus J. Kiker,¹★, James F. Steiner², Cecilia Garraffo², Mariano Mendez³, and Liang Zhang^{4,5}

¹ Sunny Hills High School, 1801 Lancer Way, Fullerton, CA 92833, USA

² Center for Astrophysics | Harvard & Smithsonian, 60 Garden St. Cambridge, MA 02138, USA

³ Kapteyn Astronomical Institute, University of Groningen, P.O. BOX 800, 9700 AV Groningen, The Netherlands

⁴ Key Laboratory for Particle Astrophysics, Institute of High Energy Physics, Chinese Academy of Sciences, Beijing 100049, People's Republic of China

⁵ ~~Center for Field Theory and Particle Physics and Department of Physics, Fudan University, 200438 Shanghai, China~~

Accepted XXX. Received YYY; in original form ZZZ

ABSTRACT

Astronomy is presently experiencing profound growth in the deployment of machine learning to explore large datasets. However, the phenomena of transient quasi-periodic oscillations (QPOs) which appear in power density spectra of many X-ray binary system observations represents an intriguing area of astronomy heretofore not explored with machine learning. In light of this, we propose and experiment with novel methodologies for predicting the presence and properties of QPOs to make the first ever detections and characterizations of QPOs with machine learning models. We base our findings on raw energy spectra and processed features derived from energy spectra using an abundance of data from the *NICER* and *Rossi X-ray Timing Explorer* space telescope archives for two black hole low mass X-ray binary sources, GRS 1915+105 and MAXI J1535-571. Our goal is to advance these non-traditional methods as a foundation for using machine learning to discover global inter-object generalizations between and provide unique insights about energy and timing phenomena to assist with the ongoing challenge of unambiguously understanding the nature and origin of QPOs. Additionally, we have developed a publicly available Python machine learning library, QPOML, to enable further Machine Learning aided investigations into QPOs.

Key words: accretion, accretion disks — black hole physics — stars: individual (GRS 1915+105, MAXI J1535+571) — X-rays: binaries

★ E-mail: thaddaeus@emailforpublicto.see

1 INTRODUCTION

At the ends of their lives, massive stars “do not go gentle into that good night” (Thomas 1952). Instead, if their initial mass exceeds $\sim 8 M_{\odot}$, core collapse leads to spectacular Type II supernovae (Schlegel 1995). If the compact remnant remains bound or becomes bound to a non-degenerate companion star, the result can be a neutron star or black hole remnant (Gilmore 2004). In special cases, this object maintains a non-degenerate partner, and together these may form an X-ray binary (XRB) system, in which the non-degenerate star engages in mass-exchange with its compact partner (Tauris & van den Heuvel 2006). Such systems are characterized by accretion from the donor star, through accretion disks (Shakura & Sunyaev 1973) and are the sources for jets (Gallo et al. 2005; van den Eijnden et al. 2018) and winds (Neilsen 2013; Castro Segura et al. 2022). Additional exotic phenomena like thermonuclear surface burning (Bildsten 1998) have also been observed with neutron stars. Both BH and NS systems are both observed to emit thermal X-ray radiation with temperatures ~ 1 keV that is understood to arise from the conversion of gravitational potential to radiative energy. Neutron stars can produce thermal emission at their surfaces, and the optically thick, geometrically thin accretion disks around both NSs and BHs can produce strong thermal X-ray emission (Shakura & Sunyaev 1973). Furthermore, black hole XRBs both also show hard X-ray flux coming from Compton up-scattering of thermal disk emission by a cloud of hot electrons around the compact source known as the corona (Galeev et al. 1979; White & Holt 1982). Comptonized emission is commonly modeled by a power law relationship $N(E) \propto E^{-\Gamma}$, where Γ is the photon index (McClintock & Remillard 2006). Strongly-Comptonized spectra commonly exhibit reflection features like a fluorescent, relativistically broadened 6.4 keV Fe $K\alpha$ line (Fabian et al. 1989) and ~ 30 keV Compton hump (Ross & Fabian 2005). These systems can be transient in activity and undergo evolution in spectral states (Gardenier & Uttley 2018), ranging from hard, to intermediate, and to soft (McClintock & Remillard 2006), which are coupled with mass-accretion rate (Done & Gierliński 2004), spectral hardness or thermal dominance, and thereby position on a hardness-intensity or color-color diagram track (Ingram & Motta 2019), and the presence/absence of quasi-periodic oscillations (QPO) of the observed X-ray radiation (McClintock & Remillard 2006). These QPOs are detected as narrow peaks in power-density spectra (Homan & Belloni 2005). In the past thirty years, numerous theories, including but not limited to relativistic precession (Stella & Vietri 1998), precessing inner flow (Ingram et al. 2009), corrugation modes (Kato & Fukue 1980), accretion ejection instability (Tagger & Pellat 1999), and propagating oscillatory shock (Molteni et al. 1996) have been advanced to explain the occurrence of QPOs in black hole, as well as neutron star, XRB systems. Yet, there is not consensus as to which model is most plausible. In black-hole systems, most of the observed QPOs have been at low frequencies (LF) ≤ 30 Hz (Belloni et al. 2020). Only a small subset has BHXRBS have exhibited high-frequency QPOs (HFQPO). The former is further subdivided canonically into three classes (Casella et al. 2005): Type-A QPOs are the rarest, sometimes appearing in the intermediate or soft state as broad, low amplitude features centered between 6-9 Hz and usually lacking harmonic companions (Ingram & Motta 2019). Type-B QPOs are more common, and can be seen during the short soft intermediate state and have shown some connection with Jet behavior (Gao et al. 2017). Finally, type C QPOs are the most common, and can be detected as narrow ($Q > 8$) features in nearly all states with harmonic companions (Fragile et al. 2016). Their fundamental frequencies range from ~ 0.1 -30 Hz depending on state, and almost always correlate strongly with spectral features like Γ and luminosity (Motta et al. 2015). As for HFQPOs, we recommend readers to (Motta et al. 2011), (Stella & Vietri 1999) and (Abramowicz & Kluźniak 2001). QPOs are also observed in neutron star systems (Wang 2016). We focus on LFQPOs from BXRBS in this paper and recommend Wang (2016) for a review of neutron star specific QPOs and Ingram & Motta (2019), Jonker et al. (1999), Kato (2005), and Revnivtsev et al. (2001) for further discussion of QPOs in XRBs in general. All in all, hundreds of XRBs have been observed since the discovery of Sco X-1 (Giacconi et al. 1962; Liu et al. 2007; Corral-Santana, J. M. et al. 2016).

Although machine learning has been applied to a number of problems related XRBs, e.g. to classify accretion states (Sreehari & Nandi 2021), predict compact object identity (Pattanaik et al. 2021), and study gravitational waves (Schmidt et al. 2021), this represents tens of thousands of observations that have heretofore not been explored with machine learning to the ends of detecting QPOs. Therefore, in this work we seek to develop a methodology for using machine learning to detect QPOs: we believe that within the context of astrophysics, our theoretical understanding of QPOs and their exotic progenitor systems could benefit from insights this approach could provide (Fudenberg & Liang 2020). The rest of this paper is structured as follows: in Section 2 we describe the observations upon which we base our work. Following this, in Section 3 we describe the energy and spectral fitting procedures we employ to produce input/output data from these observations for the machine learning models and methods which we detail in Section 4. We present our results in Section 5, and we discuss these results contextually in Section 6. Finally, we conclude in Section 7. Additional work concerning demonstrating QPOML and model comparison are presented in following appendices.

2 OBSERVATIONS

2.1 GRS 1915+105

GRS 1915+105 is a well studied galactic LMXRB system composed of a $12.4^{+2.0}_{-1.8} M_{\odot}$ primary and K III secondary (Greiner et al. 2001) on a 34 d period located $8.6^{+2.0}_{-1.6}$ kpc from the Earth (Reid et al. 2014). The secondary star in this system overflows its Roche lobe. GRS 1915+105 was one of the first microquasar jet systems, with (apparent) superluminal motion detected from a ballistic jet launched with an inclination 70 ± 2 (Mirabel & Rodríguez 1994). Since its discovery in 1992 (Castro-Tirado et al. 1992), this somewhat peculiar source has displayed unique timing and spectral patterns which have been organized into 14 separate variability classifications depending on its variability state (Hannikainen et al. 2005). With its 16-year archive of observations of this source we considered all data from the Rossi X-ray Timing

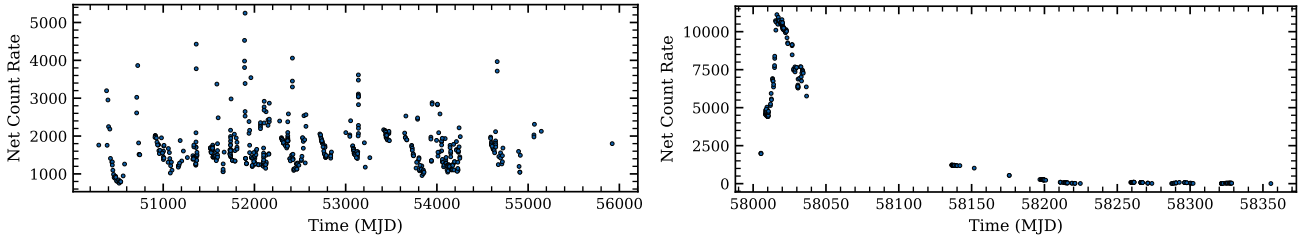


Figure 1. Light curves composed of GRS 1915+105 (left) and MAXI J1535-571 (right) observations used in this work. Net count rates are calculated as the sum of the background subtracted counts divided by observation time for every observation of each source. Note the persistent nature of GRS 1915+105 versus the transient flare of MAXI J1535-571 (reflaring epochs of MAXI J1535-571 are not included given the lack of QPOs detected there in previous works).

Explorer (RXTE) Proportional Counter Array (PCA; 2 – 60 keV) that are also included in Zhang et al. (2020). These include a great number of detections of type C QPOs between 1996 and 2012. Energy and power-density spectra (PDS) have been derived from binned, event, and GoodXenon data as described in Zhang et al. (2020). Briefly, PDS have been constructed by averaging 128 s long intervals at 1/128 s time resolution, normalized according to Leahy et al. (1983), and Poisson noise subtracted (Zhang et al. 1995). Of the 625 timing observations in Zhang et al. (2020), we have 554 matching energy spectra.

2.2 MAXI J1535-571

MAXI J1535-571 was discovered by the MAXI/GSC nova alert system as a hard X-ray transient system undergoing outburst in 2017 by Negoro et al. (2017a), and it was first suggested to be black hole system by Negoro et al. (2017b). Since discovery, it has been suggested as a ~ 10.39 low-mass XRB, ~ 5 kpc distant (Sridhar et al. 2019). It has displayed state transitions (Nakahira et al. 2018), reflaring events (Cúneo et al. 2020), and hysteresis during its main outburst (Parikh et al. 2019). Furthermore, it has been determined to possess a near-maximal dimensionless spin parameter of $a = \frac{cJ}{GM^2} > 0.99$ (Miller et al. 2018; Liu et al. 2022). To study this source we use data from the International Space Station mounted, soft X-ray (0.5–12 keV) observatory Neutron star Interior Composition ExploreR (NICER) (Gendreau et al. 2012) which has unequaled spectral-timing capabilities in soft X-rays.

We have filtered our *NICER* data following standard practices, excluding South Atlantic Anomaly passages in order to identify continuous good time intervals (GTIs) which are extracted and analyzed individually. Data from detectors 14, 34, and 54 have been excised owing to a propensity for elevated noise or spurious events in those detectors. Additionally, for each GTI, the average event rates of overshoot, undershoot, and X-ray events are compared amongst the detector ensemble, and any detector which is > 15 median absolute deviation (MAD) is also excised for that GTI¹. All spectra have been corrected for deadtime losses (generally $< 1\%$). *NICER* backgrounds have been computed using the 3C50 background model (Remillard et al. 2022), as well as using a proprietary and similar background model which replaces the 3C50’s “hrej” and “ibg” indexing with cutoff-rigidity “COR_Sax” and overshoot-rate indexing. We have removed any data with a background count rate ≥ 5 counts/s, exclude observations for which the source-to-background count ratio is < 10 , and reject observations with exposure times $t < \sim 60$ s. Additionally, we require least 5000 net source counts to ensure reliable energy and power-density spectral results, and we consider the remaining data sufficiently bright and insensitive to the selection between these similar background models. Energy spectra have been rebinned from the 10 eV PI channels by a factor ranging from 2–6 in order to oversample *NICER*’s energy resolution by a factor $\gtrsim 2$, while also requiring a minimum of 5 counts per bin. From 1 – 4096 Hz, PDS are computed using events in the energy range from 0.2 – 12 keV, for a light-curve sampling at 2^{-13} s ($\approx 122\mu$ s). PDS are computed individually and averaged together using 4s segments for $t < 160$ s and 16s segments for $t \geq 160$ s. Below 1 Hz, PDS are computed by averaging together results for 128s segments for $t \geq 128$ s 64s segments for $64 \leq t < 128$ s and 4s segments for $t < 64$ s. The resulting PDS is then logarithmically rebinned in $\sim 3\%$ frequency intervals, the Poisson noise subtracted, and the $\text{rms}^2 \text{ Hz}^{-1}$ normalization adopted.

Although we have less MAXI J1535-571 observations with QPOs for analysis (in large part due to the source’s transient nature), one benefit of using *NICER* as over RXTE data for this source (if we could have used RXTE data) is that *NICER* spectral channels do not suffer from gain drift over epochs like RXTE PCA (which affected energy-channel conversions), and thus we can use the *NICER* energy spectra as raw inputs to our regression and classifier models, in addition to the engineered features discussed in Section 3 and Section 4.2.

3 DATA ANALYSIS

3.1 Energy Spectra

As previously mentioned and discussed in more detail in Section 4.2, we base our detection of QPOs on energy spectra and processed features from the energy spectra. Thus, to generate the processed spectral features we fit the energy spectra for both sources with XSPEC

¹ The MAD is a robust statistic which is insensitive to outliers. 15 MAD corresponds to approximately 10σ for a Gaussian-distribution.

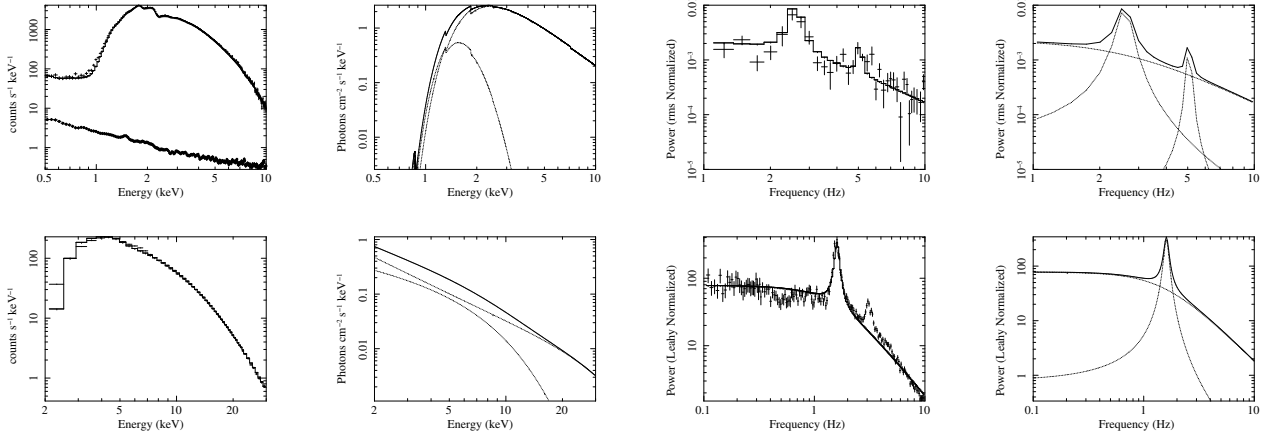


Figure 2. Example energy and power density spectra and models for MAXI J1535 observation 1050360105 – 21 on the top and the same for GRS 1915+105 observation 40116 – 01 – 01 – 07 on the bottom. For each row, from left to right the first plot shows the energy spectrum and folded `tbabs*(nthcomp+diskbb)` model, the second shows energy spectrum model alone, the third shows the power density spectrum in the relevant frequency range, and the fourth shows the best fit Lorentzian PDS model alone. Best fit QPO features have been superimposed over zero centered Lorentzians used to model the power-density continuum.

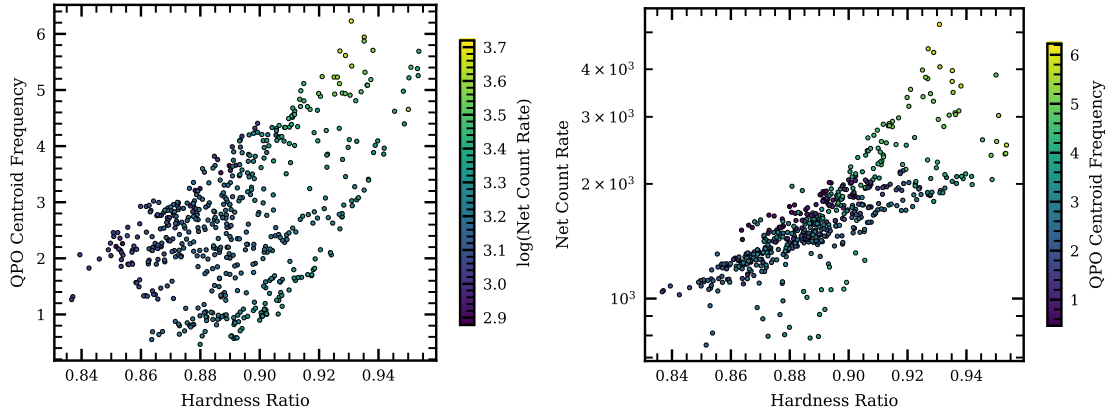


Figure 3. QPO fundamental frequency as a function of hardness ratio (defined in Section 3) and net count rate per PCU as well as net count rate as a function of QPO fundamental frequency and hardness ratio for observations of the black hole source GRS 1915+105 (see also García et al. (2022)). The relative parameter degeneracies between parameters in these plots demonstrate the benefits from making predictions based on higher dimensional input spaces.

version 12.12.0 (Arnaud et al. 1999) using the three component model `tbabs*(diskbb+nthcomp)`, which represents a Tuebingen-Boulder absorbed multi-temperature blackbody and thermally Comptonized continuum (Mitsuda et al. 1984; Zdziarski et al. 1996; Kubota et al. 1998; Życki et al. 1999). We fixed the equivalent hydrogen column densities to canonical values of 6×10^{22} atoms cm^{-2} for GRS 1915+105 and 3.2×10^{22} atoms cm^{-2} for MAXI J1535-571 based on Sreehari et al. (2020) and Cúneo et al. (2020), respectively, with solar abundances in accordance with Wilms et al. (2000) and Verner et al. (1996) cross-sections. We tied the `nthcomp` seed photon temperature to T_{in} of `diskbb` for both sources, and let high energy rollover (electron temperature) freely vary between 4 – 40 keV for GRS 1915+105 and 4 – 250 keV during fitting for MAXI J1535-571, basing these ranges on Zhang et al. (2022) and Dong et al. (2022), respectively. For GRS 1915+105, we ignore channels < 2.5 keV or > 25 keV during fitting, calculate net count rate from the resulting range, and compute hardness as the sum of the ratio of the background subtracted channel net count rates for the ranges in Zhang et al. (2022), i.e. $\frac{[13-60] \text{ counts s}^{-1}}{[2-7]+[13-60] \text{ counts s}^{-1}}$. Regarding MAXI J1535-571, we note the presence of instrumental residuals in the 1.7 – 2.3 keV *NICER* range, likely related to *NICER*’s Au mirror coating and residual in the Si K α fluorescence peak, and following Miller et al. (2018), we address these by excluding the 1.7 – 2.3 keV energy band from the spectral fitting process, and otherwise fit the range 0.5 – 10.0 keV. We compute net count rate normalized to the number of *NICER* detectors, and hardness ratios for MAXI J1535-571 observations as the proportion of the total net count rate contributed by the 3.0 – 10.0 keV range, i.e. $\frac{[3.0-10.0] \text{ counts s}^{-1}}{[0.5-1.7]+[2.3-3.0]+[3.0-10.0] \text{ counts s}^{-1}}$. Altogether, for both sources we use the net count rate, hardness ratio, asymptotic power-law photon index, `nthcomp` normalization, inner disk temperature, and `diskbb` normalization for input parameters, which we discuss in more detail in Section 4.2.

3.2 Power Density Spectra

$$A(f) = \frac{K(\frac{\sigma}{2\pi})}{(f - f_0)^2 + (\frac{\sigma}{2})^2} \quad (1)$$

Throughout this work, all QPOs for both sources are parameterized as Lorentzian distributions given by Equation 1, where f is frequency in Hertz, σ is full width at half maximum (FWHM), and K is normalization, as per [Arnaud et al. \(1999\)](#). In the case of GRS 1915+105, QPO properties are obtained by fits to PDS following [Zhang et al. \(2020\)](#). These are considered significant when their significance (ratio of the QPO power integral divided by its 1σ error) > 3 or quality factor ($Q = \frac{v_0}{\text{FWHM}}$) > 2 ([Nowak et al. 1999](#)), provided their frequency does not change significantly with source intensity, *intra-observation*. Our primary use for this GRS 1915+105 data is to train machine learning regression models to predict the properties of fundamental (i.e. the fundamental frequency of the QPO feature) QPO features, since *only* data with matching QPO detections are used in our GRS 1915+105 machine-learning analysis. In all, this corresponds to 554 QPOs. In contrast to this approach of fitting individual QPOs solely for regression, we use the energy and timing data from MAXI J1535-571 to explore both classification of observations into binary states of QPO presence/absence as well as multiclass QPO cardinality states² based on binned raw energy spectra and processed features, as well as ~~the for~~ the prediction of the properties for both the fundamental and frequently appearing harmonic in the PDS based on binned energy spectra and spectral parameterizations derived from energy spectra. Our QPO detection method for MAXI J1535-571 is slightly different than that of GRS 1915+105, however. Specifically, we determine the presence and properties of QPOs in PDS from MAXI J1535-571 by first fitting two zero-centered Lorentzian distributions to PDS and then iteratively fitting a third Lorentzian over a logarithmically linear sampled set of 268 frequencies f between 1 and 20 Hz, where width is kept $\sigma < \frac{f}{10}$ for an initial fit, and then freed for a subsequent refined fitting step. If a peak of qualifying distance and threshold is identified with the `scipy` function `find_peaks` ([Pedregosa et al. 2011](#)) in the resulting distribution of $-1 \cdot \chi^2$ fit-statistic with peak height greater than the $\Delta 10$ Akaike Information Criterion ([Akaike 1998](#)). Finally, a visual inspection is required to accept a QPO candidate detection (to avoid potential spurious detections, e.g., at the frequency boundary). In 68 of observations the fundamental is accompanied by the first harmonic; in 14 of the observations it is alone; and in 188 of the observations no distinct QPO is detected.

4 MACHINE LEARNING METHODS

4.1 Model Selection

In machine learning, models can be broadly divided by two sets of classification: (i) whether they operate in a supervised or unsupervised manner; and (ii) whether they are built for classification or regression ([Bruce & Bruce 2017](#)). Since we are providing our models with explicit targets for loss minimization, our approach falls under the umbrella of supervised learning ([Singh et al. 2016](#)), and as we are attempting to connect spectral information about XRBs with real-valued output vectors that describe QPOs in their power-density spectra, we also fall under (multi-output) regression ([Xu et al. 2019](#)). In selecting our machine learning models for regression, we seek those that natively support multi-output regression, incorporate capabilities for mitigating overfitting, have precedents of working successfully with medium to small sized data sets, and natively communicate feature importances. Additionally, we seek to evaluate a collection of models against each other in light of the No-Free-Lunch-Theorem ([Wolpert 2002](#); [Lones 2021](#)).

Based on these criteria, we settle on a set of tree-based models and their descendants, specifically decision trees ([Breiman 1984](#)), random forests ([Breiman 2001](#)), extremely randomized trees ([Geurts et al. 2006](#)), and XGBoost ([Chen & Guestrin 2016](#)). Here we provide a brief summary of these models for context. decision trees are the original tree-based regression model which operate by inferring discriminative splits in data and making predictions via a series of “if-then-else” decisions ([Breiman 1984](#)). random forests are more powerful derivatives of decision trees, and are based on an ensemble of decision trees trained via bootstrap aggregation ([Breiman 1996, 2001](#)). By incorporating predictions from such an ensemble, random forests reduce prediction variance while increasing overall accuracy when compared to a single decision tree ([Lakshminarayanan 2016](#)). extremely randomized trees (also known as extra trees) are similar to random forests in this respect but operate with more randomization during the training process, as instead of employing the most discriminative thresholds within feature spaces for splits, extremely randomized trees select the best performing randomly drawn thresholds for splitting rules ([Geurts et al. 2006](#); [Pedregosa et al. 2011](#)). Finally, XGBoost builds upon stochastic gradient boosting for improved performance in terms of speed and efficiency compared to its predecessors like AdaBoost ([Chen & Guestrin 2016](#); [Azmi & Baliga 2020](#)). One important distinction between XGBoost and random forests/extremely randomized trees is that only the former employs boosting, which is the often performance enhancing practice of successively fitting models to training cases with large predictive errors ([Friedman 2002](#)). However, in the absence of proper hyperparameter optimization, XGBoost stands at a greater risk of overfitting. Details on training and optimization are detailed in Section 4.3, where we also discuss our steps to avoid this ([Bruce & Bruce 2017](#)).

Together, these represent some of the most powerful yet lightweight machine learning models available, and meet our criteria for multi-output regression ([Xu et al. 2019](#)), robustness to overfitting ([Boinee et al. 2008](#); [Ampomah et al. 2020](#)), success with small/medium sized datasets ([Floares et al. 2017](#)), and feature importances ([Yasodhara et al. 2021](#)). An additional benefit of these models is that they are natively supported

² Also called multinomial classification ([Bouveyron et al. 2019](#)), when number of classes totals to ≥ 3

by the `TreeExplainer` method in the SHAP Python package (Lundberg & Lee 2017), which frees us from common pitfalls related to impurity and permutation based feature importances, which we discuss in more detail in Section 6. Overall, we explore all the above models in addition to ordinary linear regression (to provide a base performance comparison) for the regression cases, but focus on random forest and logistic regression (Berkson 1944) for classification cases.

4.2 Feature Engineering

As Casari & Zheng (2018) detail, feature engineering is the process of transforming raw data to maximize predictive performance. After experimenting with different formats, we settled on the following in order to use derived features from spectral fits or raw spectral data as predictors and timing features as outcomes. We will hereafter refer to and experiment with two types of input data for our models: the first are rebinned net energy spectra, which we discuss below and will simply call “energy spectra.” The second type is the combination of XSPEC model-fit parameters and spectrum derived features like net count rate and hardness which we will designate the “engineered features” input type. When using engineered features for inputs, we format our input data as a matrix composed of vectors containing the net count rate, hardness ratio, asymptotic power-law photon index, `nthcomp` normalization, inner-disk temperature, and `diskbb` normalization for every observation. Hereafter, we refer to and present these values by the letters $\{A, B, C, D, E, F, G\}$ as shorthand. This input structure is visualized in Equation 2.

$$\text{IN}_{m \times 7} = \begin{bmatrix} A_1 & B_1 & C_1 & D_1 & E_1 & F_1 & G_1 \\ \vdots & \vdots & \vdots & \vdots & \vdots & \vdots & \vdots \\ A_m & B_m & C_m & D_m & E_m & F_m & G_m \end{bmatrix} \quad (2)$$

This format can be extended to any n -dimensional number of features, which we take advantage of when using raw energy spectra as input data. For the case of MAXI J1535-571, we compare the predictive performance of the models and provide different insights by using raw spectral data in the form of count rate values from 19 channels, 0.5 keV wide apiece spanning the energy range $[0.5 - 10.0]$ directly as the input vectors within the input matrix, similar to Pattnaik et al. (2020). This coarse spectral input strikes a balance between sparsity and precision, allowing us to determine importances for specific 0.5 keV ranges while not overwhelming the models with too many input features given the overall sample size (Raudys & Jain 1991; van de Schoot & Miočević 2020). With regards to regression, our QPO output matrix is similarly formatted as a vector matrix, with rows that match by index to vectors in the input matrix, but with an important addition regarding ordering (detailed below). A significant challenge relates to the prediction of not only the presence versus absence of QPOs in a given PDS, as well as (for present cases) the specific number of QPOs and the physical parameters of each QPO present. Over the course of an outburst, the number of QPOs present can change, as these are transient phenomena (Remillard et al. 2006; Ingram & Motta 2019). We account for this challenge of variable output cardinality by first identifying all QPO occurrences associated with an observation. Then, we order these occurrences and their features in a vector of length $L = N_f \times \max(N_s)$, where N_f is the number of features describing every QPO (e.g. $N_f = 3$ for frequency, width, and amplitude), and N_s is the maximum number of simultaneous QPOs observed in any particular PDS in a data set. We then structure each output vector as a repeating subset of features for every QPO contained, and order these internal QPO parameterizations by frequency. If one or more of these occurrences are not detected in a PDS, their feature spaces in the vector are populated with zeros. This allows us to circumvent the aforementioned difficulty with variable output cardinality, because the models will learn during training to associate indices populated with zeros as QPO non-detections (Chollet 2017). As with input features, Equation 3 provides a visualization of the general QPO matrix output returned by our model, where each row corresponds to one observation matched with a row in the input matrix (both out of m total observations).

$$\text{OUT}_{m \times n} = \begin{bmatrix} f_{1,1} & \sigma_{1,1} & K_{1,1} & \dots & f_{1,n} & \sigma_{1,n} & K_{1,n} \\ \vdots & \vdots & \vdots & \ddots & \vdots & \vdots & \vdots \\ f_{n,1} & \sigma_{n,1} & K_{n,1} & \dots & f_{n,n} & \sigma_{n,n} & K_{n,n} \end{bmatrix} \quad (3)$$

In the case of MAXI J1535-571, the maximum number of QPOs simultaneously observed in a PDS is two, and each QPO is described in terms of its frequency, width, and amplitude, so the output matrix takes the shape $\text{OUT} = m \times 6$. Since we only regress for the fundamental in the GRS 1915+105 PDS, its output matrix takes the form $\text{OUT} = m \times 3$. Prior to reformatting the data in this manner, we applied a columnar min-max standardization to the XSPEC, and hardness input features, as well as the QPO Lorentzian output features, which linearly transformed each distribution into a $[\max(x'), \min(x')] = [0.1, 1]$ range (as opposed to the traditional $[0 - 1]$ range given our decision to denote QPO non-detections with zero values) while preserving their shapes, according to Equation 4 (Kandanaarachchi et al. 2019).

$$x' = \frac{x - \min(x)}{\max(x) - \min(x)} \times \frac{\max(x') - \min(x')}{\min(x')} \quad (4)$$

This step is necessary to prevent features with larger absolute amplitudes receiving undue weight, and it also frees the models from dependency on measurement units (Akanbi et al. 2015; Han et al. 2012). We did not apply this standardization step to channel count and net

count rate input features, however, as the imposition of *a priori* theoretical limits to these features is not as readily justifiable (Pattnaik et al. 2020).³

4.3 Training, Validation, and Hyperparameter Tuning

To better understand our models in different data combinations and minimize statistical noise, while guaranteeing every observation gets included in a training, as well as at a separate time, test instance, we employ a repeated k -fold cross-validation strategy (Olson & Delen 2008; Vanwinckelen & Blockeel 2012) for model evaluation (as opposed to a default proportion-based train-test split). According to this procedure, our data is first randomly split into $k = 10$ folds. Given the relative class imbalance in the MAXI J1535-571 data in favor of observations without QPOs, for MAXI J1535-571. As a result, the folds for both regression and classification cases are also stratified during splitting, which means each fold maintains the same proportion of observations with QPOs (Ma & He 2013). Then, every model is evaluated on each unique fold after being trained on the remaining folds, with the individual k -fold performance taken as the mean of these evaluations across the ten folds. We repeat this process ten times (randomly shuffling the data between each iteration), and the final score for each model is calculated as the mean performance across the ten k -fold instances (Kuhn & Johnson 2019). Random numbers are kept the same between models to make sure each is trained/tested on the same data within each fold, and to ensure fair comparison between these models, each was subject to automatic and individualized hyperparameter tuning via grid search prior to this evaluation (Dangeti 2017). In the case of XGBoost, for example, this included modulation of learning rate η , ℓ_1 regularization, number of ensemble tree estimators, and maximum tree depth to minimize overfitting while maximizing predictive performance. For purposes of concise presentation, we only present figures generated from the tenth, which forms a pseudo test set for discussion (e.g. Figure 4, Figure 6, Figure 7, etc.). Beyond these, there are some results shown like the receiver operator characteristic (ROC) curves in Figure 8 that depict averaged results across repetitions and folds to give an aggregated understanding of referenced concepts that takes inter-fold variance into account.

4.4 Feature Selection

Through feature selection, it is generally important to deal with potential multicollinearity by calculating Variance Inflation Factors (VIF) and removing features with VIF values $\gtrsim 5$ (Kline 1998; Sheather 2008). However, we have chosen not to remove potentially collinear features prior to regression for the following reasons: first, the tree based models like random forest that we focus on are by design robust from the effects of multicollinearity (Strobl et al. 2008; Chowdhury et al. 2021). Second, since multicollinearity only affects the estimated coefficients of linear models, but not their predictive ability, applying a linear model to potentially collinear data is perfectly reasonable in our case, as we are using the linear model solely as a baseline against which we will compare the predictive capabilities of the more complicated random forest model; i.e. as we are applying the linear model, we are not interested in its components (Lieberman & Morris 2014; Mundfrom et al. 2018). We will, however, revisit multicollinearity when we interpret feature importances in Section 5.

5 RESULTS

5.1 Regression

As demonstrated in Figure 4, our tree-based models outperform linear regression in every regression case, regardless of source or input feature type. Interestingly, as shown in Figure 7, linear regression also seriously struggles to correctly assign 0 values to observations lacking QPOs for both processed and rebinned energy spectra input data, a problem not faced by the other models (except random forest with rebinned energy spectra to a lesser degree). Furthermore, linear regression always has higher dispersion in the relationship between actual and predicted QPO frequency. Yet, despite their unified superiority versus linear regression, the machine learning models do differ significantly within fold amongst themselves, as shown in Figure 4, Figure 6, and Figure 7. Specifically, although decision tree provides notable a improvement in dispersion between true and predicted values, as well as a slope between these closer to unity, it is by far bested by random forest, extra trees, and XGBoost. Two additional interesting divergences in model performance occur between source and between input type. Regarding the former, all models trained and evaluated on GRS 1915+105 data have more overall dispersion and slopes tending further away from unity in their mapping between true and predicted frequency when compared to the same models for MAXI J1535-571 QPOs with processed input features. This can be clearly seen when comparing Figure 6 versus the top row in Figure 7. The superior performance of the algorithms on MAXI J1535-571 are surprising for several reasons: first, with GRS 1915+105 the models never face the problem of false negatives or false positives because there are no QPO-absent data in this set. In contrast, MAXI J1535-571 observations are of varying composition, imbalanced in favor of QPO absence. Second, GRS 1915+105 has around two times more total observations, and around six times more observations with QPOs than MAXI J1535-571; in most cases training models on more data leads to corresponding increases in accuracy (Kalinin & Foster 2020; Brefeld et al. 2020). However, this assumption may not hold in instances like this, where models are being tested on different objects,

³ Standardization prior to splitting data into train and test sets does not impair our model's predictive validity when input features are derived from XSPEC because its pre-adjusted inputs will always be constrained within the theoretical bounds applied during standardization for each feature (e.g. Γ will always initially range between $x - y$).

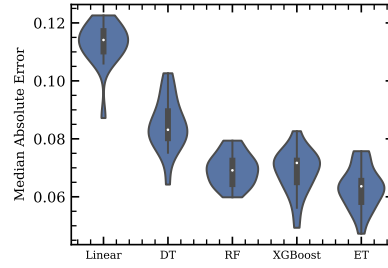


Figure 4. Gaussian kernel density estimate violin plot representations of aggregated median absolute error for each tested model across $k = 10$ validation folds repeated $r = 3$ times on GRS 1915+105 (spectral input) data.

as there may exist fundamentally stronger/more pronounced associations between spectral and QPO in one of the systems. The most likely reason for the inferior performance on GRS 1915+105 QPOs is that the underlying relationships between the input and output QPO features are likely more convoluted for GRS 1915+105, which is understandable given GRS 1915+105 has long been known to have complicated variability states, and is in fact a bit of an oddball among black-hole systems. Additionally, potential confusion could arise because the models fitted on fundamental QPOs only in GRS 1915+105 intentionally lack the freedom to predict aspects about harmonics, which could lead to these models to potentially confuse signals for harmonics with fundamentals. Finally, to evaluate the performance of the multioutput aspect of the regression, we carry out pairwise nonparametric two-sided goodness-of-fit Kolmogorov-Smirnov (KS) tests on permutations of QPO parameter residual arrays (Massey 1951; KS- 2008), and fail in all instances to reject the hypothesis that any pair of distributions of residual arrays between actual and predicted QPO parameters are not drawn from the same distribution ($p > 0.76$ for all GRS 1915+105 and $p > 0.99$ for all MAXI J1535-571 residual pair permutations, regardless of input type). This shows that the models do not favor any particular QPO parameter in their regression and instead regress for each with statistically insignificant differences in accuracy (i.e. accuracy is not different for QPO features, both for the fundamental, as well as the harmonic when present). As for the second interesting divergence in model performance (by input type), surprisingly there is a pronounced difference in model performance when these regression models are trained on processed features as opposed to rebinned energy spectra: in all model cases, dispersion and slope both drastically worsen when models rely on the rebinned energy spectra directly. This demonstrates that although the models could hypothetically learn some lower level representation of the concepts of hardness, overall net count rate, etc. from the data and not require the engineered features, with the amount of data provided engineered features provide significant additional insight for the models to base decisions on that exceeds what is provided by energy spectra alone. This would be an interesting idea to investigate with deep learning methods which would far exceed these classical models' ability to learn abstractions in the data through automated feature extraction (Nadeau & Bengio 2004).

5.2 Classification

At least for MAXI J1535-571, binary classification of QPO absence/presence appears to be a fairly trivial task, as shown by the confusion matrices of the first repetition tenth folds in Figure 8. Additionally, as Figure 8 also shows, our logistic regression classifier corollary to linear regression performs just as well as random forest in terms of accuracy and other classification metrics when trained on processed input data, with negligible difference for rebinned energy spectra as well. This is corroborated by corresponding ROC curves also shown in Figure 8. ROC curves show how a model has optimized between specificity (on the abscissa) and recall (also known as sensitivity; on the ordinate), with the ideal model displaying an ROC curve enclosing an area under curve (AUC) of 1 (Bruce & Bruce 2017). The curves in Figure 8 represent the average ROC and AUC values with $1 \pm \sigma$ deviations across all folds and repetitions evaluated. Both logistic regression and random forest decrease in average AUC when trained on rebinned energy spectra, but the decrease is most dramatic for logistic regression. In Figure 9, we also present multiclass classification results for multinomial logistic regression and random forest based on processed and rebinned energy spectra input data in Figure 9. In the case of processed input data, random forest clearly outperforms logistic regression, but both models actually experience noted decreases in accuracy when tasked with predicting multiple outputs corresponding to the actual number of QPOs in a MAXI J1535-571 observation based on rebinned energy spectra input. In fact, in the case of energy spectra inputs, random forest actually performs worse than logistic regression. Overall, the decreased performance of both models here is likely do to the class imbalance in the data set (as mentioned in Section 3), which gives the models very few single QPO observations to use as training data per round.

6 DISCUSSION

6.1 Feature Importances and Interpretation

Feature importances refer to the relative attributed weights a model gives to different input features (Saarela & Jauhiainen 2021). In other words, they are measures for how helpful different features are for the model in making correct predictions, regardless of whether these predicted values are categorical or real-valued (Fisher et al. 2018). Before we discuss these, however, we will briefly describe our efforts to

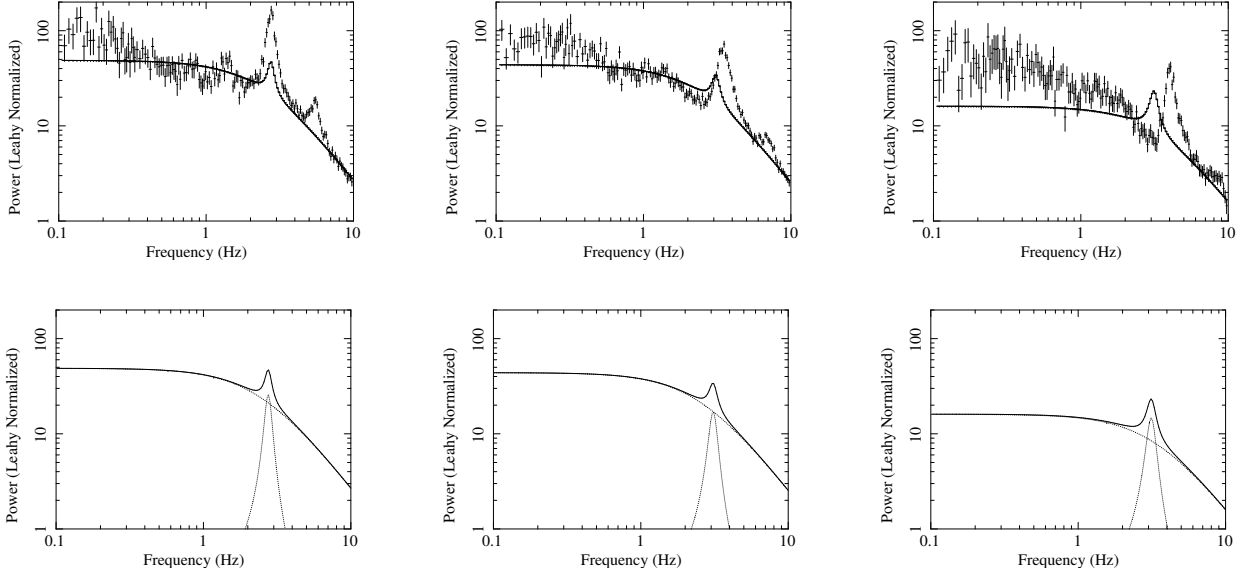


Figure 5. Example PDS with over plotted QPO predictions for the GRS 1915+105 observations 80701-01-54-02, 50703-01-28-01, 50703-01-24-01 ordered by column left to right from least (best-fitting), median, to greatest (worst) Pythagorean sum of normalized errors on the three predicted QPO Lorentzian parameters (with corresponding models alone in bottom row). Note that the seeming diminished height of the predicted QPOs is actually a consequence of how they were determined in the processing procedure, and in the case of the best observation 80701-01-54-02, the amplitude only differs by less than 0.3% from the “true” amplitude value it was predicting, as the derived amplitudes had reduced amplitudes originally.

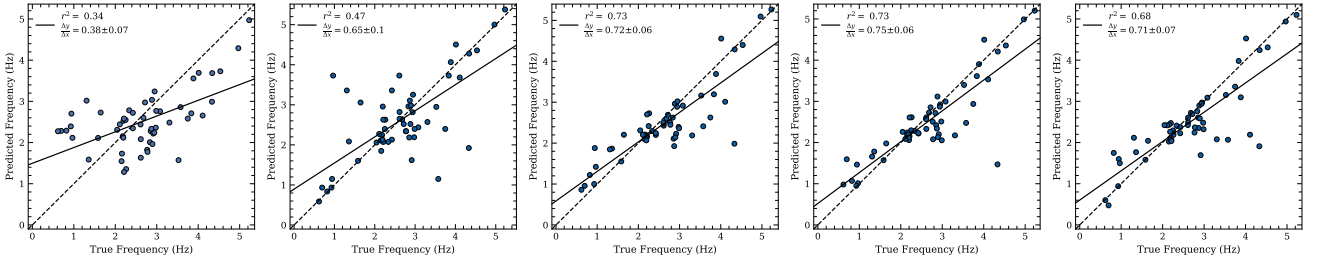


Figure 6. A results regression plot for all QPOs predicted in the tenth for the source GRS 1915+105 as predicted (from left to right) by linear regression, decision tree, random forest, extra trees, and XGBoost. Note how the best models, random forest, extra trees, and to a lesser extent XGBoost, both minimize dispersion between true and predicted values (as quantified by r^2), while simultaneously producing the most 1:1 relationships between them (as quantified by best fit slope).

ensure the interpretability of our machine learning models. Interpretability is defined parsimoniously by [Miller \(2017\)](#) as the degree to which a human can understand the cause of a decision. Since most of our models are intrinsically complex (except for linear and logistic regression and decision trees), we seek *post hoc* interpretability through feature importances ([Vieira & Digiampietri 2022](#)). These values should not be interpreted as substitutes for other e.g. parametric importances, because they seek to explain how a machine learning model learns and interacts with its data. However, we believe that properly calculated feature importances may offer alternative helpful insight about the origins of QPOs, and we therefore take steps to avoid common pitfalls associated with these measures. For example, although it is common to discuss default impurity-based feature importances, this approach is flawed it is both biased towards high-cardinality numerical input features, as well as computed on training set statistics, which means it may not accurately generalize to held-out data ([Pedregosa et al. 2011](#)). Additionally, although permutation importances are commonly put forward as a superior alternative, these suffer from multicollinearity, as in the process of permuting single features, an impactful feature could be erroneously ascribed as having little-to-no effect on model performance if it has high correlation with another feature ([Strobl et al. 2007](#); [Nicodemus et al. 2010](#); [Hooker et al. 2019](#)). Therefore, we chose to determine feature importances with the contemporary TreeSHAP algorithm as implemented in the Python package shap by [Lundberg & Lee \(2017\)](#). This model extends game theoretic coalitional Shapley values to calculate SHapley Additive exPlanations (SHAP) in the presence of multicollinearity by incorporating conditional expected predictions ([Shapley 1952](#); [Lundberg & Lee 2017](#); [Molnar 2022](#)). As hinted earlier and detailed in [Lundberg & Lee \(2017\)](#) and [Molnar \(2022\)](#), an additional benefit of using tree based models is that through tree traversal and dynamic programming the computational cost for computing SHAP values is brought down from exponential time $O(2^n)$ to $O(n^2)$ polynomial time. Similar to Section 5, we calculate feature importances by treating the models from the tenth fold in the first repetition as if they were taken from the test set, and

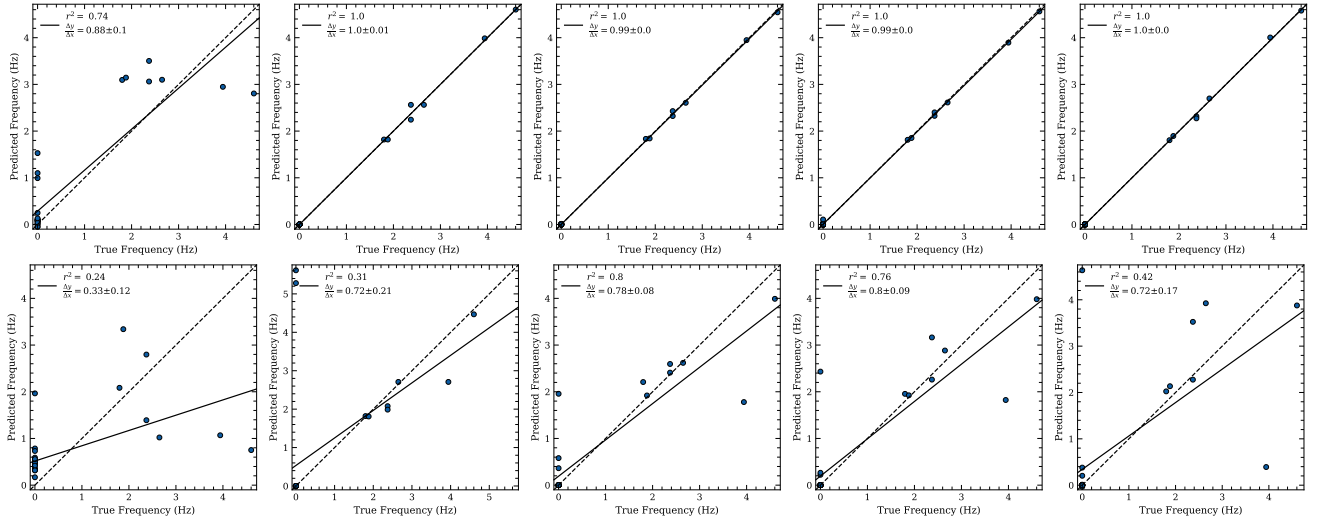


Figure 7. Same as Figure 6, except for MAXI J1535-571 observations. Note the increased dispersion and much less 1:1 relationships between true and predicted values for every model using the upper row (processed feature inputs) and corresponding bottom row (rebinned energy spectra as inputs). The lesser number of points in these plots stems from both the smaller sample size of MAXI J1535-571 observations, as well as the clustering of values correctly predicted as zeros at the point (0, 0) where points cannot be seen individually in this plot.

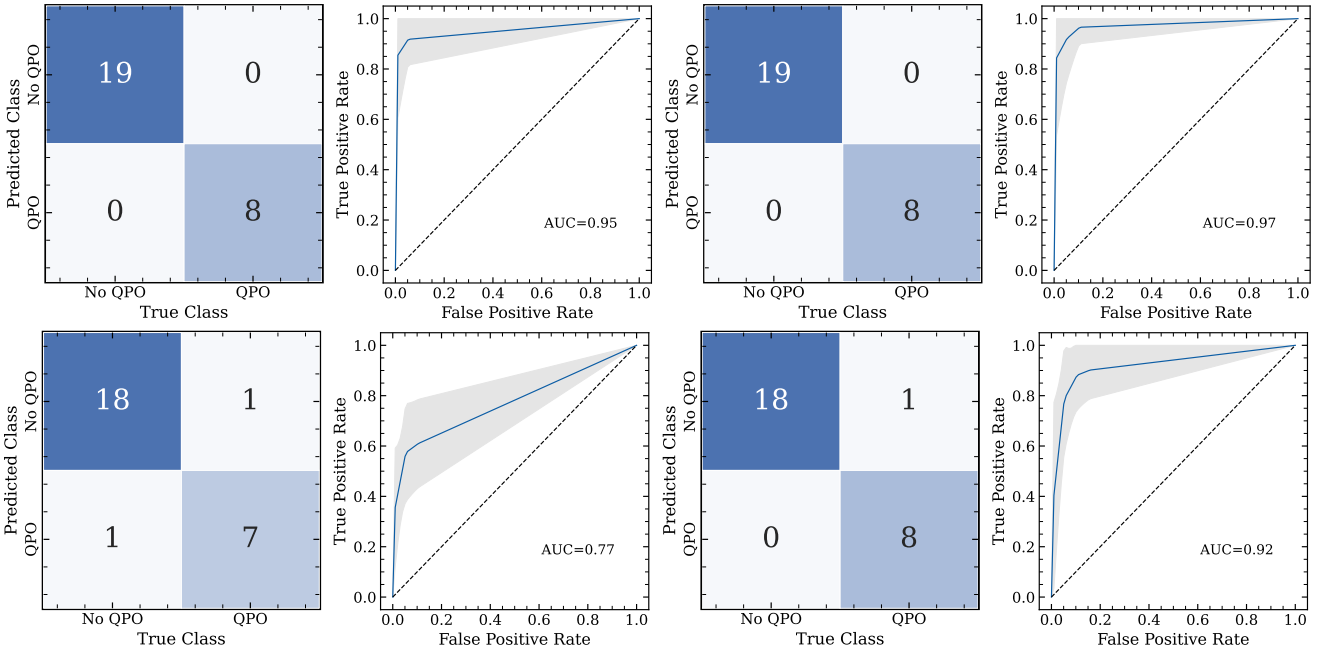


Figure 8. Confusion matrices and ROC Curves with labeled AUC values for binary classification cases. The left pairs correspond to logistic regression, whereas the right correspond to random forest. The confusion matrices are taken from the first tenth fold, whereas the ROC curves are averaged across all folds with $\pm 1\sigma$ deviance denoted by the grey regions. Note the superior performance of the models working from processed inputs in the top row compared to their rebinned energy spectra input analogues in the bottom row.

averaging their $\phi_i(f, x)$ from Equation 5, which represents the weighted average of differences in model performance when a feature is present versus absent for all subsets $z' \subseteq x'$.

$$\phi_i(f, x) = \sum_{z' \subseteq x'} \frac{|z'|!(M - |z'| - 1)!}{M!} [f_x(z') - f_x(z' \setminus i)] \quad (5)$$

One of the most important things shown by Figure 10 and 11 is that there are significant interesting differences between the feature importances attributed to the processed features for GRS 1915+105 and MAXI 1535-571, which may be related to the nuances of the process driving QPOs in these systems. For example, in GRS 1905+105, net count rate and hardness ratio are clearly the most important features, after which importance falls precipitously and remains uniformly modest for the rest, with this proportional decrease ranging from a factor of three

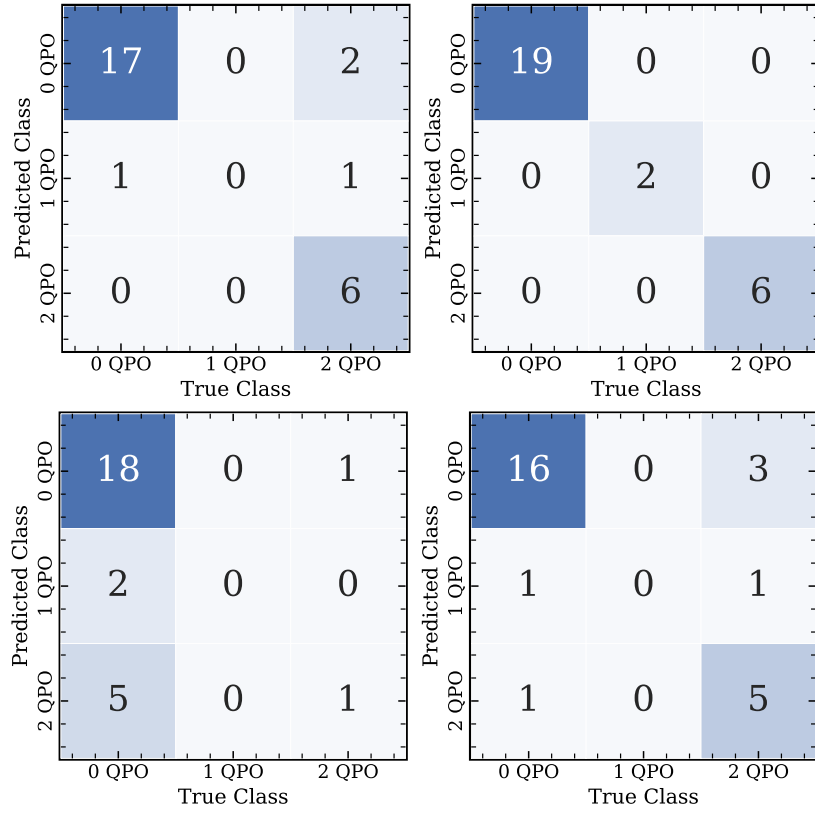


Figure 9. Confusion matrices for multiclass MAXI J1535-571 output, where the left column corresponds to logistic regression, the right column to random forest, the top row to processed input features, and the bottom row to rebinned energy spectra input features. Note the pronounced poorer accuracy for both models (except for random forest on processed inputs) as compared to the binary case presented in Figure 8.

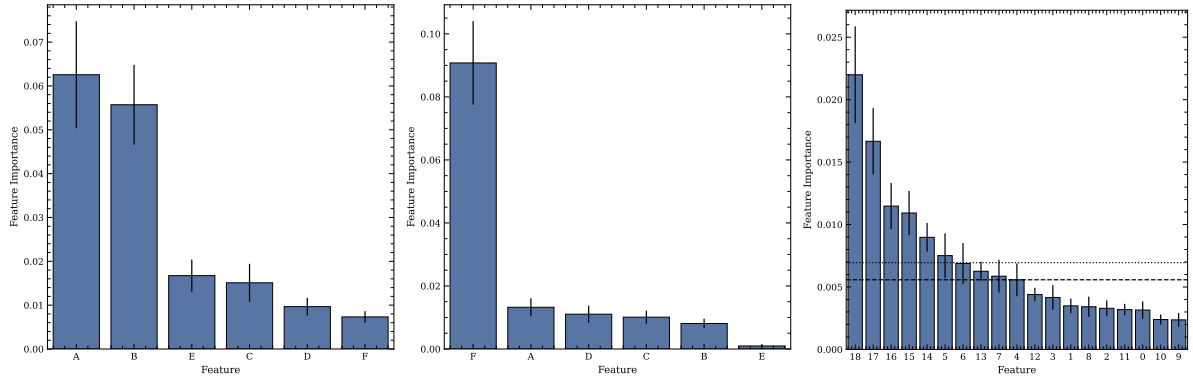


Figure 10. Tree-SHAP calculated average of absolute value SHAP feature importances for the most accurate predictive regression models for GRS 1915+105 engineered inputs (left, extra trees), MAXI J1535-571 engineered inputs (middle, extra trees), and MAXI J1535-571 energy spectra inputs (right, extra trees). The error bars on each importance correspond to 99% confidence intervals on mean importances, the dashed line the median importance of all features, and the dotted line the mean of the same. Note how features corresponding to hard channel count rates are significantly more important than the median and mean feature importance, and the differences in importance attribution between GRS 1915+105 and MAXI J1535-571 for engineered inputs.

for `nthcomp` asymptotic power law to six for `nthcomp` and `diskbb` normalization. Because we have used SHAP values for importance, we can rule out the un-importance of these features stemming from multicollinearity or training set artifacts, which means they could *potentially* be related to curious physical related conditions. However, there is no ambiguity about the importance of net count rate and hardness, because an XRB outburst’s Q-shaped state-evolution in hardness-intensity diagrams (HIDs) is known to also be indicative of changes in timing (e.g., QPO) properties as tracked in HIDs (Motta et al. 2015; Motta 2016). This is also in agreement with findings of Figure 2 from (García et al. 2022), in which QPO frequency for GRS 1915+105 is shown to vary with a somewhat inverse relationship with hardness ratio across mostly horizontal and vertical gradients in inner disk temperature and power law index, respectively.

In contrast to GRS 1915+105, the feature importances for both the best regression and classification models on processed MAXI J1535-571

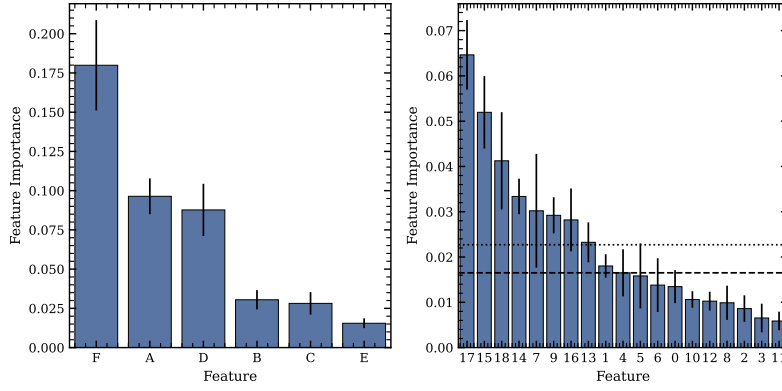


Figure 11. Similar to Figure 10, except for the best classification models for MAXI J1535-571 binary output based on engineered inputs (left, random forest), and energy spectral inputs (right, random forest). Note the similar dominance of features corresponding to hard energy channels as seen in Figure 10

input features favor a single feature above all others: `diskbb` normalization. This quantity (ignoring relativistic and plasma corrections) approximately corresponds to the projected area of the inner-disk on the sky: $N_{\text{disk}} = (\frac{R_{\text{in}}}{D_{10}})^2 \cos(\theta)$, where R_{in} the apparent inner disk radius in km, D_{10} is the distance to the source in 10 kpc units, and θ the angle of the disk (Arnaud et al. 1999). This prominent importance is intriguing because it implies a dependence between QPO presence and frequency on `diskbb` normalization and therefore inner disk radius. This is corroborated by Garg et al. (2022), who find QPO frequency correlates significantly with the inner disk radius for MAXI J1535-571 in data provided by *AstroSat* according to the power law relationship $\nu_{\text{QPO}} \propto \dot{M} R_{\text{in}}^p$, where \dot{M} is mass-accretion rate (Rao et al. 2016). However, (Garg et al. 2022) do not find a clear relationship between `diskbb` normalization and QPO frequencies in the $\sim 1.6 - 2.8$ Hz range. Overall, the similarity in feature importances for engineered features for regression and classification in MAXI J1535-571 shows that the same features that are important in determining the parameterizations of QPOs are those important in determining their presence vs absence. Regarding the feature importances derived from the energy spectra, the highest energy channels are the most important for both regression and classification, with the five most important channel counts rates for each coming from the equivalent $[9.5 - 10)$, $[9.0 - 9.5)$, $[8.5 - 9.0)$, $[8.0 - 8.5)$ and $[7.5 - 8.0)$ keV channels for regression and $[9.0 - 9.5)$, $[9.5 - 10.0)$, $[8.5 - 9.0)$, $[8.0 - 8.5)$ and $[3.0 - 3.5)$ keV channels for classification. Notably, for both classification and regression only hard channels ≥ 3 keV have importances significantly greater than the mean and median importances for all features in their respective sets at the 99% confidence level. The fact that the high-energy spectral data is most informative of the QPOs is interesting and we speculate that this may be related to the fact that QPOs manifest more prominently at higher energies above the disk’s peak temperature. A broader perspective which generalizes these relationships to other BH systems is of high interest, but outside the scope of this work.

6.2 Statistical Model Comparison

As mentioned in Section 4, we included an ordinary least squares model as a benchmark for their utilization. As Figure 4, Figure 6, and 7 demonstrate, each of our models outperform linear regression. In order to assess the significance of the improvements, we employ the Nadeau & Bengio (2004) formulation of the frequentist Diebold-Mariano corrected paired t-test (Diebold & Mariano 1995),

$$t = \frac{\frac{1}{k \cdot r} \sum_{i=1}^k \sum_{j=1}^r x_{ij}}{\sqrt{(\frac{1}{k \cdot r} + \frac{n_{\text{test}}}{n_{\text{train}}}) \hat{\sigma}^2}} \quad (6)$$

where $k = 10$ and represents the number of k-fold validation folds, $r = 10$ and equals the number of times we repeated the k-fold procedure, x is the performance difference between two models, and $\hat{\sigma}^2$ represents the variance of these differences (Pedregosa et al. 2011). It is necessary to correct the t -values in this manner because the performances of the models are correlated with each fold upon which they are tested, as some folds may make it harder for one of or all of the models to generalize, whereas others make it easier, and thus the collective performance of the models varies. The results of these pairwise tests for all permutations of two models on both sources is shown in Table 1.

We additionally implement the Bayesian Benavoli et al. (2016) approach, which allows us to calculate the *probability* that a given model is better than another, using the Student distribution formulated in Equation (7):

$$\text{St}(\mu; n - 1, \bar{x}, (\frac{1}{n} + \frac{n_{\text{test}}}{n_{\text{train}}}) \hat{\sigma}^2) \quad (7)$$

where n is the total number of samples, \bar{x} is the mean score difference, and $\hat{\sigma}^2$ is the Nadeau & Bengio (2004) corrected variance in differences (Pedregosa et al. 2011). Both sets of these pairwise tests are also shown in Table 1.

Based on these tests, it is clear that extra trees significantly out performs all other models, and interestingly, that each model that follows it

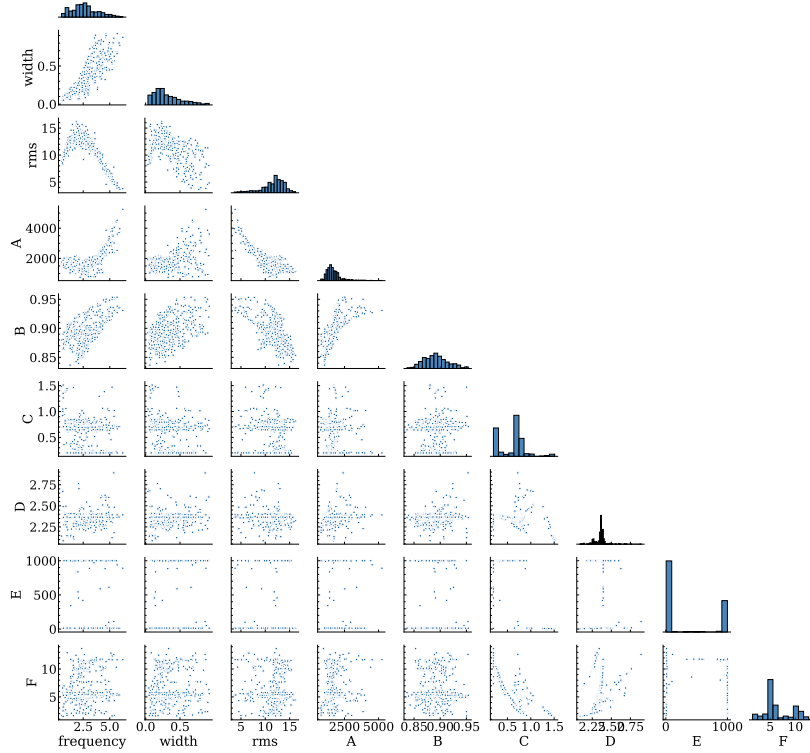


Figure 12. A pairplot displaying the pairwise relationships between engineered input and Lorentzian QPO output parameters for all GRS 1915+105 data. The letters in A – F correspond to the net count rate, hardness ratio, asymptotic power-law photon index, `nthcomp` normalization, inner-disk temperature, and `diskbb` normalization features, respectively.

in decreasing order of performance is significantly better than the remaining models following it, confirming the findings in Figure 4, except for the random forest XGBoost pair. Based on these findings it appears that these classical machine learning models have been able to fairly accurately optimize for individual sources. However, although extra trees may perform best in these individual source scenarios, it remains yet to be seen whether these classical models will be generalizable for accurate cross-source analyses or if other models like neural networks will be required..

7 CONCLUSION

In this paper we have advanced novel approaches utilizing machine learning algorithms to link energy spectral properties (as both rebinned raw energy spectra and alternatively via engineered features derived from spectral fits) with the presence and properties of QPOs prominent in power-density spectra of two low-mass X-ray binary black hole systems. Specifically, we tested a selection of tree-based classical machine learning models using engineered features derived from energy spectra to predict QPO properties for fundamental QPOs in the black hole GRS 1915+105, and such derived features as well as raw rebinned energy spectra to characterize fundamental and harmonic QPOs in the black hole MAXI J1535-571. Additionally, we trained classification algorithms on the same data to predict the presence/absence of QPOs, as well as the multiclass QPO state of MAXI J1535-571 observations. We compared the performance of the machine learning models against each other, and found extremely randomized trees to perform best in all regression situations for both sources. Additionally, we compared every model against simplistic linear (regression) and logistic (classification) models as well, finding the machine learning models outperformed their linear counterpart in all regression cases, with linear regression notably struggling to correctly identify observations lacking QPOs. The main findings from this study are:

- (i) All tested regression models yielded significantly better results on MAXI 1535-571 versus GRS 1915+105 data, despite the latter having 6x more data with QPOs and no issue with QPO absent observations. We attributed this to the multitude of unusual variability classes unique to GRS 1915+105 among [Huppenkothen et al. \(2017\)](#).
- (ii) Kolmogorov-Smirnov tests on permutations of QPO parameter residuals showed the best fitting regression model, Extra Trees, does not favor any particular QPO parameter and instead predicts for all with equal accuracy, including those for harmonics.
- (iii) Using rebinned raw spectral data as opposed to XSPEC derived features resulted in significantly worse performance for regression, binary classification, and multiclass classification on MAXI J1535-571 observations.

(iv) To enhance computational efficiency and ensure importance credibility, we calculated `TreeShap` feature importances immune to multicollinearity and found that for processed input features, extremely randomized trees found the most significant features for GRS 1915+105 were net count rate and hardness ratio, whereas the same model predicting for MAXI J1535-571 found `diskbb` normalization most important, which suggests dependence on physical inner disk radius in this case.

(v) We found the same rebinned channels which are the most important in determining the parameterizations of QPOs are also those that are most important in determining their presence versus absence in MAXI J1535-571 energy spectral data. Furthermore, for energy spectra, we found hard channels are the most important for both regression and classification, which aligns with the understanding of higher energy QPO manifestation above peak disk temperatures

We based our work on our QPOML Python library, from input and output matrix construction and preprocessing, to hyperparameter tuning, model evaluation, and plot generation, which were all conveniently streamlined for application and both (i) executed as “under-the-hood” as possible while remaining user accessible; and (ii) easily extendable to any number of QPOs and any number of scalar observation features for any number of observations from any number of sources. We preview QPOML in Appendix 8, and provided source code as well as documentation for it on GitHub.

8 ACKNOWLEDGEMENTS

We thank Virginia A. Cuneo for a helpful conversation early in this work, Michael Corcoran and Craig Gordon for assistance with some early technical issues. Finally, we thank Travis Austen with help recovering a significant amount of our work from a damaged virtual machine disk, and Brandon Barrios for Windows Subsystem for Linux advice. This work was made possible by the *NICER* and *RXTE* missions, as well as data from the High Energy Astrophysics Science Archive Research Center (HEASARC) and NASA’s Astrophysics Data System Bibliographic Services.

Facilities: *NICER*, *RXTE*

Software: *Software:* *AstroPy* (Astropy Collaboration et al. 2013, 2018), *Keras* (Chollet et al. 2015), *Matplotlib* (Hunter 2007), *NumPy* (Harris et al. 2020), *Pandas* (Wes McKinney 2010), *SciencePlots* (Garrett 2021), *SciPy* (Virtanen et al. 2020), *scikit-learn* (Pedregosa et al. 2011), *seaborn* (Waskom 2021), and *XGBoost* (Chen & Guestrin 2016).

REFERENCES

- Abramowicz M. A., Kluźniak W., 2001, *A&A*, **374**, L19
- Akaike H., 1998, *Information Theory and an Extension of the Maximum Likelihood Principle*. Springer New York, New York, NY, pp 199–213, doi:10.1007/978-1-4612-1694-015
- Akanbi O. A., Amiri I. S., Fazeldelkordi E., 2015, in , *A Machine-Learning Approach to Phishing Detection and Defense*. Elsevier, pp 45–54, doi:10.1016/b978-0-12-802927-5.00004-6
- Ampomah E. K., Qin Z., Nyame G., 2020, *Information*, **11**
- Arnaud K., Dorman B., Gordon C., 1999, *XSPEC: An X-ray spectral fitting package*, *Astrophysics Source Code Library*, record ascl:9910.005 (ascl:9910.005)
- Astropy Collaboration et al., 2013, *A&A*, **558**, A33
- Astropy Collaboration et al., 2018, *AJ*, **156**, 123
- Azmi S. S., Baliga S., 2020.
- Belloni T. M., Zhang L., Kylafis N. D., Reig P., Altamirano D., 2020, *MNRAS*, **496**, 4366
- Benavoli A., Corani G., Demars J., Zaffalon M., 2016, arXiv e-prints, p. arXiv:1606.04316
- Berkson J., 1944, *Journal of the American Statistical Association*, **39**, 357
- Bildsten L., 1998, in Buccheri R., van Paradijs J., Alpar A., eds, *NATO Advanced Study Institute (ASI) Series C Vol. 515, The Many Faces of Neutron Stars..* p. 419 (arXiv:astro-ph/9709094)
- Boinee P., Angelis A. D., Foresti G. L., 2008, *International Journal of Computer and Information Engineering*, **2**, 2246
- Bouveyron C., Celeux G., Murphy T., Raftery A., 2019, *Model-Based Clustering and Classification for Data Science: With Applications in R*. Cambridge Series in Statistical and Probabilistic Mathematics, Cambridge University Press
- Brefeld U., Davis J., Van Haaren J., Zimmermann A., 2020, *Machine Learning and Data Mining for Sports Analytics: 7th International Workshop, MLSA 2020*, Co-located with ECML/PKDD 2020, Ghent, Belgium, September 14–18, 2020, *Proceedings. Communications in Computer and Information Science*, Springer International Publishing
- Breiman L., 1984, *Classification and Regression Trees*. (The Wadsworth statistics / probability series), Wadsworth International Group
- Breiman L., 1996, *Machine learning*, **24**, 123
- Breiman L., 2001, *Machine learning*, **45**, 5
- Bruce P., Bruce A., 2017, *Practical Statistics for Data Scientists: 50 Essential Concepts*. O’Reilly Media
- Casari A., Zheng A., 2018, O’Reilly Media, Inc., p. 218
- Casella P., Belloni T., Stella L., 2005, *ApJ*, **629**, 403
- Castro Segura N., et al., 2022, *Nature*, **603**, 52
- Castro-Tirado A. J., Brandt S., Lund N., 1992, *IAU Circ.*, **5590**, 2
- Chen T., Guestrin C., 2016, arXiv e-prints, p. arXiv:1603.02754
- Chollet F., 2017, *Deep Learning with Python*. Manning
- Chollet F., et al., 2015, *Keras*, <https://keras.io>
- Chowdhury S., Lin Y., Liaw B., Kerby L., 2021, arXiv e-prints, p. arXiv:2111.02513

- Corral-Santana, J. M., Casares, J., Muñoz-Darias, T., Bauer, F. E., Martínez-Pais, I. G., Russell, D. M., 2016, *A&A*, 587, A61
- Cúneo V. A., et al., 2020, *MNRAS*, 496, 1001
- Dangeti P., 2017, *Statistics for Machine Learning*. Packt Publishing
- Diebold F. X., Mariano R. S., 1995, *Journal of Business Economic Statistics*, 13, 253
- Done C., Gierliński M., 2004, *Progress of Theoretical Physics Supplement*, 155, 9
- Dong Y., Liu Z., Tuo Y., Steiner J. F., Ge M., García J. A., Cao X., 2022, *MNRAS*, 514, 1422
- Fabian A. C., Rees M. J., Stella L., White N. E., 1989, *MNRAS*, 238, 729
- Fisher A., Rudin C., Dominici F., 2018, *J* 10.48550/ARXIV.1801.01489
- Floares A., Ferisgan M., Onita D., Ciuparu A., Calin G., Manolache F., 2017, *Int J Oncol Cancer Ther*, 2, 13
- Fragile P. C., Straub O., Blaes O., 2016, *MNRAS*, 461, 1356
- Friedman J. H., 2002, *Computational Statistics & Data Analysis*, 38, 367
- Fudenberg D., Liang A., 2020, *SIGames Exch.*, 18, 4–11
- Galeev A. A., Rosner R., Vaiana G. S., 1979, *ApJ*, 229, 318
- Gallo E., Fender R., Kaiser C., 2005, in Burderi L., Antonelli L. A., D’Antona F., di Salvo T., Israel G. L., Piersanti L., Tornambè A., Straniero O., eds, *American Institute of Physics Conference Series Vol. 797, Interacting Binaries: Accretion, Evolution, and Outcomes*. pp 189–196 ([arXiv:astro-ph/0501374](https://arxiv.org/abs/astro-ph/0501374)), doi:10.1063/1.2130232
- Gao H. Q., et al., 2017, *MNRAS*, 466, 564
- García F., Karpouzas K., Méndez M., Zhang L., Zhang Y., Belloni T., Altamirano D., 2022, *MNRAS*, 513, 4196
- Gardenier D. W., Uttley P., 2018, *MNRAS*, 481, 3761
- Garg A., Misra R., Sen S., 2022, *MNRAS*, 514, 3285
- Garrett J. D., 2021, *J* 10.5281/zenodo.4106649
- Gendreau K. C., Arzoumanian Z., Okajima T., 2012, in *Space Telescopes and Instrumentation 2012: Ultraviolet to Gamma Ray*. p. 844313, doi:10.1117/12.926396
- Geurts P., Ernst D., Wehenkel L., 2006, *Mach. Learn.*, 63, 3–42
- Giacconi R., Gursky H., Paolini F. R., Rossi B. B., 1962, *Phys. Rev. Lett.*, 9, 439
- Gilmore G., 2004, *Science*, 304, 1915
- Greiner J., Cuby J. G., McCaughrean M. J., Castro-Tirado A. J., Mennickent R. E., 2001, *A&A*, 373, L37
- Han J., Kamber M., Pei J., 2012, in *Data Mining*. Elsevier, pp 83–124, doi:10.1016/b978-0-12-381479-1.00003-4
- Hannikainen D. C., et al., 2005, *A&A*, 435, 995
- Harris C. R., et al., 2020, *Nature*, 585, 357
- Homan J., Belloni T., 2005, *Ap&SS*, 300, 107
- Hooker G., Mentch L., Zhou S., 2019, *arXiv e-prints*, p. [arXiv:1905.03151](https://arxiv.org/abs/1905.03151)
- Hunter J. D., 2007, *Computing in Science & Engineering*, 9, 90
- Huppenkothen D., Heil L. M., Hogg D. W., Mueller A., 2017, *MNRAS*, 466, 2364
- Ingram A., Motta S. E., 2019, *New Astronomy Reviews*
- Ingram A., Done C., Fragile P. C., 2009, *MNRAS*, 397, L101
- Jonker P. G., van der Klis M., Wijnands R., 1999, *ApJ*, 511, L41
- 2008, *Kolmogorov–Smirnov Test*. Springer New York, New York, NY, pp 283–287, doi:10.1007/978-0-387-32833-1_214
- Kalinin S., Foster I., 2020, *Handbook On Big Data And Machine Learning In The Physical Sciences (In 2 Volumes)*. World Scientific Series On Emerging Technologies, World Scientific Publishing Company
- Kandanaarachchi S., Muñoz M. A., Hyndman R. J., Smith-Miles K., 2019, *Data Mining and Knowledge Discovery*, 34, 309
- Kato S., 2005, *PASJ*, 57, L17
- Kato S., Fukue J., 1980, *PASJ*, 32, 377
- Kline R., 1998, *Principles and Practice of Structural Equation Modeling. Methodology in the Social Sciences*, Guilford Publications
- Kubota A., Tanaka Y., Makishima K., Ueda Y., Dotani T., Inoue H., Yamaoka K., 1998, *PASJ*, 50, 667
- Kuhn M., Johnson K., 2019, *Applied Predictive Modeling*. Springer New York
- Lakshminarayanan B., 2016, *PhD thesis*, UCL (University College London)
- Leahy D. A., Elsner R. F., Weisskopf M. C., 1983, *ApJ*, 272, 256
- Lieberman M., Morris J., 2014, 40, 5
- Liu Q. Z., van Paradijs J., van den Heuvel E. P. J., 2007, *A&A*, 469, 807
- Liu Q., Liu H., Bambi C., Ji L., 2022, *MNRAS*, 512, 2082
- Lones M. A., 2021, *arXiv e-prints*, p. [arXiv:2108.02497](https://arxiv.org/abs/2108.02497)
- Lundberg S. M., Lee S.-I., 2017, in Guyon I., Luxburg U. V., Bengio S., Wallach H., Fergus R., Vishwanathan S., Garnett R., eds, Vol. 30, *Advances in Neural Information Processing Systems*. Curran Associates, Inc.
- Ma Y., He H., 2013, *Imbalanced Learning: Foundations, Algorithms, and Applications*. Wiley
- Massey F. J., 1951, *Journal of the American Statistical Association*, 46, 68
- McClintock J. E., Remillard R. A., 2006, in *Vol. 39, Compact stellar X-ray sources*. pp 157–213
- Miller T., 2017, *arXiv e-prints*, p. [arXiv:1706.07269](https://arxiv.org/abs/1706.07269)
- Miller J. M., et al., 2018, *The Astrophysical Journal*, 860, L28
- Mirabel I. F., Rodríguez L. F., 1994, *Nature*, 371, 46
- Mitsuda K., et al., 1984, *PASJ*, 36, 741
- Molnar C., 2022, *Interpretable Machine Learning*, 2 edn
- Molteni D., Sponholz H., Chakrabarti S. K., 1996, *ApJ*, 457, 805
- Motta S. E., 2016, *Astronomische Nachrichten*, 337, 398
- Motta S., Muñoz-Darias T., Casella P., Belloni T., Homan J., 2011, *Monthly Notices of the Royal Astronomical Society*, 418, 2292
- Motta S. E., Casella P., Henze M., Muñoz-Darias T., Sanna A., Fender R., Belloni T., 2015, *MNRAS*, 447, 2059
- Mundfrom D., Smith M., Kay L., 2018, *General Linear Model Journal*, 44, 24
- Nadeau C., Bengio Y., 2004, *Machine Learning*, 52, 239
- Nakahira S., et al., 2018, *PASJ*, 70, 95

- Negoro H., et al., 2017a, *The Astronomer's Telegram*, 10699, 1
- Negoro H., et al., 2017b, *The Astronomer's Telegram*, 10708, 1
- Neilsen J., 2013, *Advances in Space Research*, 52, 732
- Nicodemus K. K., Malley J. D., Strobl C., Ziegler A., 2010, *BMC Bioinformatics*, 11
- Nowak M. A., Wilms J., Dove J. B., 1999, *ApJ*, 517, 355
- Olson D., Delen D., 2008, *Advanced Data Mining Techniques*. Springer Berlin Heidelberg
- Parikh A. S., Russell T. D., Wijnands R., Miller-Jones J. C. A., Sivakoff G. R., Tetarenko A. J., 2019, *ApJ*, 878, L28
- Pattanaik R., Sharma K., Alabarta K., Altamirano D., Chakraborty M., Kembhavi A., Méndez M., Orwat-Kapola J. K., 2020, *Monthly Notices of the Royal Astronomical Society*, 501, 3457
- Pattanaik R., Sharma K., Alabarta K., Altamirano D., Chakraborty M., Kembhavi A., Méndez M., Orwat-Kapola J. K., 2021, *MNRAS*, 501, 3457
- Pedregosa F., et al., 2011, *Journal of Machine Learning Research*, 12, 2825
- Rao A. R., Singh K. P., Bhattacharya D., 2016, arXiv e-prints, p. [arXiv:1608.06051](https://arxiv.org/abs/1608.06051)
- Raudys S., Jain A., 1991, *IEEE Transactions on Pattern Analysis and Machine Intelligence*, 13, 252
- Reid M. J., McClintock J. E., Steiner J. F., Steeghs D., Remillard R. A., Dhawan V., Narayan R., 2014, *ApJ*, 796, 2
- Remillard R. A., McClintock J. E., Orosz J. A., Levine A. M., 2006, *ApJ*, 637, 1002
- Remillard R. A., et al., 2022, *AJ*, 163, 130
- Revnivtsev M., Churazov E., Gilfanov M., Sunyaev R., 2001, *A&A*, 372, 138
- Ross R. R., Fabian A. C., 2005, *MNRAS*, 358, 211
- Saarela M., Jauhiainen S., 2021, *SN Applied Sciences*, 3, 1
- Schlegel E. M., 1995, *Reports on Progress in Physics*, 58, 1375
- Schmidt S., et al., 2021, *Phys. Rev. D*, 103, 043020
- Shakura N. I., Sunyaev R. A., 1973, *A&A*, 24, 337
- Shapley L. S., 1952, A Value for N-Person Games. RAND Corporation, Santa Monica, CA, [doi:10.7249/P0295](https://doi.org/10.7249/P0295)
- Sheather S. J., 2008, A modern approach to regression with R, 2009 edn. Springer Texts in Statistics, Springer, New York, NY
- Singh A., Thakur N., Sharma A., 2016, in 2016 3rd International Conference on Computing for Sustainable Global Development (INDIACom). pp 1310–1315
- Sreehari H., Nandi A., 2021, *MNRAS*, 502, 1334
- Sreehari H., Nandi A., Das S., Agrawal V. K., Mandal S., Ramadevi M. C., Katoch T., 2020, *MNRAS*, 499, 5891
- Sridhar N., Bhattacharyya S., Chandra S., Antia H. M., 2019, *MNRAS*, 487, 4221
- Stella L., Vietri M., 1998, *ApJ*, 492, L59
- Stella L., Vietri M., 1999, *Phys. Rev. Lett.*, 82, 17
- Strobl C., Boulesteix A.-L., Zeileis A., Hothorn T., 2007, *BMC Bioinformatics*, 8
- Strobl C., Boulesteix A.-L., Kneib T., Augustin T., Zeileis A., 2008, *BMC Bioinformatics*, 9
- Tagger M., Pellat R., 1999, *A&A*, 349, 1003
- Tauris T. M., van den Heuvel E. P. J., 2006, in , Vol. 39, Compact stellar X-ray sources. pp 623–665
- Thomas D., 1952, In *Country Sleep: And Other Poems*. James Laughlin
- Vanwinckelen G., Blockeel H., 2012.
- Verner D. A., Ferland G. J., Korista K. T., Yakovlev D. G., 1996, *ApJ*, 465, 487
- Vieira C. P., Digiampietri L. A., 2022. Association for Computing Machinery, New York, NY, USA, [doi:10.1145/3535511.3535512](https://doi.org/10.1145/3535511.3535512)
- Virtanen P., et al., 2020, *Nature Methods*, 17, 261
- Wang J., 2016, *International Journal of Astronomy and Astrophysics*, 6, 82
- Waskom M. L., 2021, *Journal of Open Source Software*, 6, 3021
- Wes McKinney 2010, in Stéfan van der Walt Jarrod Millman eds, *Proceedings of the 9th Python in Science Conference*. pp 56 – 61, [doi:10.25080/Majora-92bf1922-00a](https://doi.org/10.25080/Majora-92bf1922-00a)
- White N. E., Holt S. S., 1982, *ApJ*, 257, 318
- Wilms J., Allen A., McCray R., 2000, *ApJ*, 542, 914
- Wolpert D. H., 2002, *The Supervised Learning No-Free-Lunch Theorems*. Springer London, London, pp 25–42, [doi:10.1007/978-1-4471-0123-93](https://doi.org/10.1007/978-1-4471-0123-93)
- Xu D., Shi Y., Tsang I. W., Ong Y.-S., Gong C., Shen X., 2019, arXiv e-prints, p. [arXiv:1901.00248](https://arxiv.org/abs/1901.00248)
- Yasodhara A., Asgarian A., Huang D., Sobhani P., 2021, arXiv e-prints, p. [arXiv:2110.00086](https://arxiv.org/abs/2110.00086)
- Zdziarski A. A., Johnson W. N., Magdziarz P., 1996, *MNRAS*, 283, 193
- Zhang W., Jahoda K., Swank J. H., Morgan E. H., Giles A. B., 1995, *ApJ*, 449, 930
- Zhang L., et al., 2020, *MNRAS*, 494, 1375
- Zhang Y., Méndez M., García F., Karpouzas K., Zhang L., Liu H., Belloni T. M., Altamirano D., 2022, *MNRAS*, 514, 2891
- Życki P. T., Done C., Smith D. A., 1999, *MNRAS*, 309, 561
- van de Schoot R., Miočević M., 2020, *Small Sample Size Solutions: A Guide for Applied Researchers and Practitioners*. European Association of Methodology Series, Taylor & Francis
- van den Eijnden J., Degenaar N., Russell T. D., Wijnands R., Miller-Jones J. C. A., Sivakoff G. R., Hernández Santisteban J. V., 2018, *Nature*, 562, 233

```

from xgboost import XGBRegressor
import matplotlib.pyplot as plt
from qpoml import collection

collec = collection(qpo_path='./QP0.csv', context_path='./Context.csv', approach='regression')

collec.evaluate(model=XGBRegressor(), evaluation_approach='k-fold', folds=10, repetitions=3)

fig, axs = plt.subplots(1, 2, figsize=(8,4))

collec.plot_results_regression(feature_name='frequency', which=[0], ax = axs[0], fold=9)

collec.plot_feature_importances(fold=9, style='bar', ax=axs[1], hline=hline)

plt.show()

```

Figure 13. Here we present a brief demonstration of using QPOML. After QPO features have been aggregated and saved in a formatted csv file, the path to this csv file is passed to the `qpoml.collection` class to initiate a new `collection` object along with a path to the corresponding similarly formatted context csv file, which contains the input information for every observation, such as processed XSPEC or rebinned energy spectrum features. Under the hood the library automatically matches the vectors in input and output space by observation along then drops observation identifiers to order them randomly but maintain correspondence by index, while simultaneously preprocessing them and finally organizing them in the input and output matrices. Then, during evaluation, the provided model is tested across three repeated $k = 10$ cross validation runs, where the folds are automatically stratified to QPO presence/absence if this if a detected aspect of the data. Finally, the process of making plots like those in Figure 6 and Figure 10 is as easy as running the corresponding one line functions in QPOML.

APPENDIX

A. QPOML Demonstration

Table 1. Pairwise fold corrected frequentist and Bayesian statistical for all regression model comparisons discussed in Section 6, where GRS 1915+105 models are only tested on extracted (Processed) features, whereas MAXI J1535-571 models are tested on both Processed, as well as rebinned raw energy spectra features (Spectral). Abbreviations-wise, ET (extremely randomized trees), RF (Random Forest), and DT (decision tree).

Source (Input Type)	First Model Name	Second Model Name	t	p	% Chance First Better	% Chance Second Better
GRS 1915+105 (Processed)	ET	XGBoost	2.72	4.35×10^{-3}	99.3	0.7
	ET	RF	5.67	2.85×10^{-7}	100.0	0.0
	ET	DT	6.51	1.29×10^{-8}	100.0	0.0
	ET	Linear	14.27	2.88×10^{-20}	100.0	0.0
	XGBoost	RF	0.40	3.44×10^{-1}	65.4	34.6
	XGBoost	DT	4.75	7.76×10^{-6}	99.99	0.01
	XGBoost	Linear	10.29	1.21×10^{-14}	100.00	0.0
	RF	DT	4.63	1.17×10^{-5}	99.99	0.01
	RF	Linear	14.43	1.78×10^{-20}	100.0	0.0
	DT	Linear	6.19	4.25×10^{-8}	100.0	0.0
MAXI J1535-571 (Processed)	ET	DT	1.16	1.26×10^{-1}	86.9	13.1
	ET	XGBoost	1.81	3.78×10^{-2}	95.7	4.3
	ET	RF	2.19	1.64×10^{-2}	97.9	2.1
	ET	Linear	12.16	2.89×10^{-17}	100.0	0.0
	DT	XGBoost	0.02	4.90×10^{-1}	50.9	49.1
	DT	RF	0.12	4.52×10^{-1}	54.8	45.2
	DT	Linear	11.28	5.22×10^{-16}	100.0	0.0
	XGBoost	RF	0.14	4.46×10^{-1}	55.4	44.6
	XGBoost	Linear	11.53	2.36×10^{-16}	100.0	0.0
	RF	Linear	12.41	1.31×10^{-17}	100.0	0.0
MAXI J1535-571 (Spectral)	ET	DT	1.11	1.35×10^{-1}	86.0	14.0
	ET	RF	3.25	1.01×10^{-3}	99.8	0.2
	ET	XGBoost	4.62	1.25×10^{-5}	99.99	0.01
	ET	Linear	9.59	1.80×10^{-13}	100.0	0.0
	DT	RF	0.44	3.31×10^{-1}	66.8	33.2
	DT	XGBoost	0.81	2.12×10^{-1}	78.5	21.53
	DT	Linear	6.40	2.07×10^{-8}	100.0	0.0
	RF	XGBoost	0.51	3.07×10^{-1}	69.1	30.9
	RF	Linear	6.92	3.05×10^{-9}	100.0	0.0
	XGBoost	Linear	7.51	3.45×10^{-10}	100.0	0.0

B. Model Comparison